

Potassium-40 geoneutrinos detection and the Earth's large-scale structures imaging by directional geoneutrino detection

Haozhe Sun, Zhe Wang,* and Shaomin Chen

Department of Engineering Physics, Tsinghua University, Beijing 100084, China

Center for High Energy Physics, Tsinghua University, Beijing 100084, China and

Key Laboratory of Particle & Radiation Imaging (Tsinghua University), Ministry of Education, Beijing 100084, China

(Dated: April 2, 2026)

Geoneutrinos, the electron (anti)neutrinos generated in decays or decay chains of the radioactive elements within the Earth, primarily ^{40}K , ^{238}U , and ^{232}Th , serve as a unique probe for the inner chemical composition of the Earth. A directional geoneutrino detection method with a Cherenkov liquid scintillator is investigated in this work. The neutrino-electron elastic scattering in the scintillator is employed to detect geoneutrinos. The direction reconstruction resolution for neutrinos is studied based on previous measurements and simulations. The intrinsic neutrino background from the Sun is suppressed with an optimized solar angle cut. The 3σ sensitivity to discover the potassium neutrinos is 2.8 kiloton-years. The potential to reach a non-uniform geoneutrino image with the Earth's large-scale structures is also studied. The required exposure is 10.6 kiloton-years to reject a uniform geoneutrino distribution by 3σ .

Keywords: geoneutrino, Cherenkov liquid scintillator, potassium neutrino, Earth imaging

I. INTRODUCTION

A. Neutrino geoscience

Geoneutrinos originate from the decay of radioactive elements within the Earth. They primarily come from three radioactive elements: uranium, thorium, and potassium (U, Th, and K). Measuring the fluxes of various geoneutrinos and imaging the Earth's large-scale structures will provide us with a wealth of knowledge [1]. First, the geoneutrino flux corresponds directly with the radiogenic heat flux. Subtracting it from the total terrestrial surface heat flux (about 46 TW), we can infer the residual heat from the Earth's primordial gravitational collapse [2]. Second, U and Th are refractory elements that condense out of a nebular disk at high temperatures and are empirically observed in equal proportions in chondrites. K is a moderately volatile element that follows a distinct condensation pathway. By measuring the potassium neutrino and knowing the abundance of K in the Earth, we can establish a volatilization curve for this planet, which allows us to infer the abundances of other volatile elements. Comparing these results with those from chondrite meteorites may provide more information in reconstructing the Earth's accretion and evolution history [2, 3]. Third, if the geoneutrinos can be used to image the planet's large-scale structure, we can gain deeper insights into the Earth. For instance, regarding the Qinghai-Tibet Plateau, the subduction of the Indian tectonic plate has formed a thick crust, and the affinity of U, Th, and K with silicate (lithophile) leads to the enrichment of heat-generating elements in the shallow geological layers. Models predict a very high flux of

geoneutrinos in this region [4, 5]. With a geoneutrino imaging of large-scale structures, we can study these models and reveal whether other unknown structures exist. Furthermore, if we can measure the flux of geoneutrinos from the mantle, we will gain valuable insights into the forces driving plate tectonics and the Earth's dynamo.

KamLAND reported the first measurement of the geoneutrinos in 2005 [6]. The most recent measurements are from KamLAND [7], Borexino [8], and SNO+ [9] experiments. The geoneutrinos were detected through the inverse beta decay (IBD) process in large liquid scintillator detectors,

$$\bar{\nu}_e + p \rightarrow e^+ + n. \quad (1)$$

In the IBD reaction, an electron antineutrino interacts with a free proton, producing a positron and a neutron. The positron deposits its kinetic energy and annihilates with an electron immediately, forming the prompt signal. The neutron subsequently thermalizes and is eventually captured by a nucleus, releasing gamma rays, forming a delayed signal. The temporal and spatial correlation between the prompt and delayed signals provides an effective selection criterion to suppress the background.

The IBD process has a detection threshold of 1.806 MeV, which is higher than the endpoint energy of the ^{40}K neutrino spectrum, at 1.31 MeV. Only uranium and thorium geoneutrinos can be detected. The directionality people can utilize from the IBD process is also quite limited [10].

Previously, it was proposed to use a Cherenkov liquid scintillator to detect the recoil electron from the neutrino-electron scattering process [11]. The proposal can be used to suppress the intrinsic background of solar neutrinos. The technique got further development in more possible solvent fluorophores [12] and the reconstruction method [13]. In this paper, we investigate

* Corresponding author: wangzhe-hep@mail.tsinghua.edu.cn

the previous idea with the Cherenkov liquid scintillator again. One problem is found in the previous simulation work. The candidate selection criteria and sensitivity calculation method have been upgraded. We found a much better sensitivity in finding the potassium neutrino, and it is also possible to generate a large-scale structure image of the Earth.

The details of this study are presented in this paper. In Sec. II, the signal prediction is described. Sec. III presents the response of the Cherenkov liquid scintillator detector. Sec. IV is for the upgraded selection criteria. The sensitivities are calculated and presented in Sec. V, and the paper is summarized in Sec. VI.

II. GEONEUTRINO SIGNAL PREDICTION

In this paper, we have the following basic experimental settings. The situation of Jinping Neutrino Experiment (JNE) is considered as the target underground laboratory and detector. JNE is located in the China Jinping Underground Laboratory (CJPL). CJPL is located in Sichuan Province with more than 2400 meters of vertical rock overburden. Muon and muon-induced backgrounds are greatly reduced. A Cherenkov liquid scintillator serves as the medium for neutrino detection. The neutrino-electron elastic scattering process is the signal process for geoneutrino detection, because it can offer directionality and give people the chance to discover potassium geoneutrinos and to do the Earth imaging. The intrinsic background is from the solar neutrinos. The backgrounds from natural radioactivity have to be taken into account, but they will be mostly reduced by detector shielding and material purification. They will be studied in separate work.

A. Coordinate system

The directionality is significant in distinguishing the geoneutrino signal from the solar neutrino background. The geoneutrino signal mainly comes from the interior of the Earth, while the solar neutrino background has a strong correlation with the Sun's direction. To characterize the difference, two sets of coordinate systems are established. The solar coordinate system focuses on the relationship with the Sun's azimuth, with the solar angle θ_{\odot} representing the angle between the recoil electron's direction and the Sun-Earth direction. The terrestrial coordinate system is fixed on the Earth, with the origin set at the detector position, the z -axis aligned along the direction from the Earth's center to the detector, and the x -axis aligned along the latitudinal direction and pointing towards the south. The angular coordinates $(\theta_{\oplus}, \phi_{\oplus})$ are defined in this coordinate system. The coordinate systems are illustrated in Fig. 1.

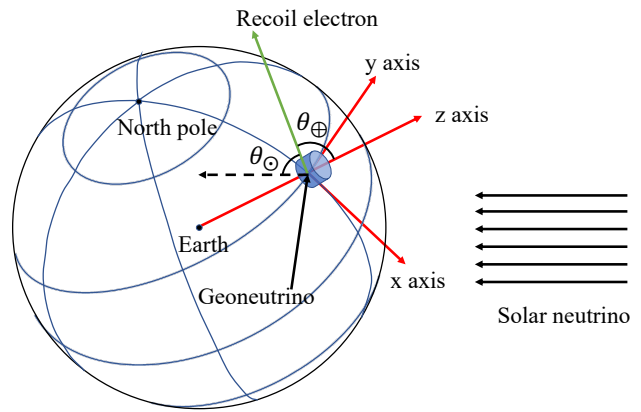


FIG. 1: The Coordinate systems. The solar coordinate system varies with the relative positions of the Earth and the Sun, while the terrestrial coordinate system is fixed on the Earth.

B. Geoneutrino prediction

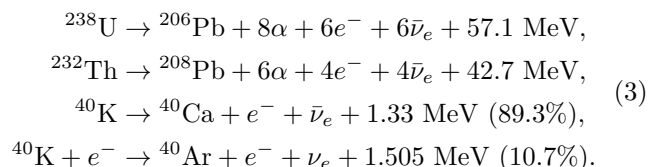
The total geoneutrino energy spectrum in Jinping of flavor α ($\alpha = e, \mu, \text{ and } \tau$), originating from an isotope i ($i = \text{U, Th, and K}$), can be written as the following formula.

$$\phi_{\alpha i}(E) = \frac{X_i \lambda_i N_A}{\mu_i} n_{\nu i} S_i(E) \times \int \frac{1}{4\pi L^2} P_{e\alpha}(E, L) \rho(\vec{r}) A_i(\vec{r}) d^3\vec{r}, \quad (2)$$

where X_i represents the mole fraction of an isotope i , λ_i represents the decay constant for i , N_A is the Avogadro's constant, μ_i is the molar mass of the isotope i , $n_{\nu i}$ represents the number of neutrinos emitted in a decay (chain), $S_i(E)$ is the normalized neutrino spectrum of isotope i , L is the distance from the location \vec{r} to Jinping detector, $\rho(\vec{r})$ is the density, and $A_i(\vec{r})$ represents the abundance of the element. $P_{e\alpha}(E, L)$ is the appearance probability of neutrino flavor x with energy E after an electron neutrino traveling through a distance L . Neutrinos and antineutrinos of all three flavors contribute to the neutrino-electron elastic scattering process.

C. Geoneutrino spectrum

The geoneutrinos are primarily from Uranium-238, thorium-232, and potassium-40:



Due to their tiny interaction cross-sections, the geoneutrinos travel almost unimpeded to the surface. The geoneutrino flux and directionality carry the information about the inner Earth. The neutrino spectrum is from the result published by Emonoto in 2005 [14]. Besides, the orbital electron capture is also considered in this research. Fig. 2 shows the (anti)neutrino spectrum from each decay. Although only

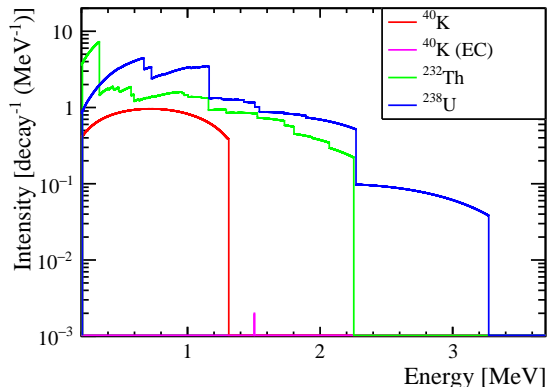


FIG. 2: Antineutrino spectrum calculated by Enomoto [14]. The monoenergetic peak of ^{40}K orbit electron capture is also shown.

0.2% of ^{40}K decays via orbital electron capture and emit an electron neutrino with energy exceeding 0.5 MeV, these neutrinos contribute approximately 4.5% signals in the energy range dominated by ^{40}K due to the relatively larger cross-section than antineutrinos.

D. Earth model

Crust 1.0 is a global crustal model that provides a detailed 3D representation of the Earth's crust [15]. The model is structured as a $1^\circ \times 1^\circ$ grid in latitude and longitude, covering the entire globe. At each grid, the crust is divided into 9 geological layers, including: ice, water, upper-, middle-, lower- sediments, and upper-, middle-, lower- crust. For each layer at every grid cell, Crust 1.0 provides key parameters including depth of boundaries, density, and crustal type. Because of the relatively high concentration of the radioactive elements in the crust and their proximity to the detector, crust-originated neutrinos account for approximately 70% of all geoneutrino signals. Beneath the crust lie the continental lithospheric mantle (CLM), depleted mantle (DM), and enriched mantle (EM). There is still no precise measurement of the element components in the mantle, and we applied a typical model as in Ref. [16]. The abundance of U, Th, and K is assumed to be uniform in a layer and the same in the same type of layers. The abundance is obtained in Ref. [4] with a medium-Q BSE assumption.

Fig. 3 shows a schematic diagram of the cross-section along the longitudinal-elevation plane. The middle figure is the expanded diagram at the latitude and longitude where the CJPL is located. The upper and lower plots are for 2° north and south of the CJPL, respectively.

E. Neutrino oscillation

Because of the mixing of neutrinos, the neutrinos change their flavor as they travel in a vacuum or matter. The survival probability of an electron antineutrino with energy E traveling a distance L in a vacuum can be written as:

$$P_{ee}(E, L) = \sum_{i=1}^3 \left| U_{ei}^\dagger U_{ie} e^{-im_i^2/2E} \right|^2, \quad (4)$$

where U is the Pontecorvo-Maki-Nakagawa-Sakata matrix (PMNS matrix). The survival probability of electron neutrinos is

$$\begin{aligned} P_{ee}(E, L) = & 1 - \cos^4 \theta_{13} \sin^2 2\theta_{12} \sin^2 2\Delta_{21} \\ & - \sin^2 2\theta_{13} \cos^2 \theta_{12} \sin^2 \Delta_{31} \\ & - \sin^2 2\theta_{13} \sin^2 \theta_{12} \sin^2 \Delta_{32}, \end{aligned} \quad (5)$$

where $\Delta_{ij} = 1.257 \times 10^{-3} \frac{\Delta m_{ij}^2 L}{E}$ and $m_{ij}^2 = |m_j^2 - m_i^2|$, with Δm_{ij}^2 in eV^2 , L in km, and E in MeV. Matter effect is taken into account. The oscillation effect is integrated over the whole Earth modeled with the PREM [17].

The distance between 1 degree of latitude is about 111 km, which is larger than the typical oscillation length, which is approximately 30 km at 1 MeV for the Δm_{12}^2 term. For the precision of the computation of $P_{ex}(E, L)$, more sub-grids are divided further from the original grid.

The parameters used in Eq. 5 are listed in Ref. [18]. For the appearance probability of μ and τ neutrinos, it is

$$P_{e\mu, e\tau}(E, L) = 1 - P_{ee}(E, L). \quad (6)$$

Fig. 4 is the predicted electron (anti)neutrino spectrum at Jinping. The results for other flavors are not shown.

F. Elastic scattering event spectrum

The differential cross-section $d\sigma(E_\nu, T_e)/dT_e$ for the neutrino-electron elastic scattering is from Ref. [19], and the scattering event rate is obtained by

$$\frac{dn(T_e)}{dT_e} = N_e \sum_k \int \frac{d\sigma_k(E_\nu, T_e)}{dT_e} \phi_k(E_\nu) dE_\nu, \quad (7)$$

where T_e is the recoil electron kinetic energy, N_e is the number of electrons of the detector target, and k represents the type of neutrino (i.e., flavor and whether

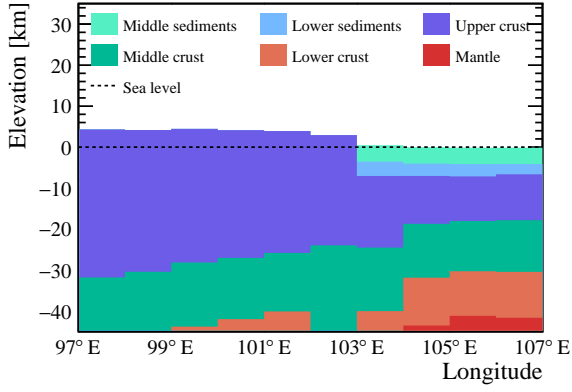


FIG. 3: Schematic diagrams of the cross-section along the longitudinal-elevation plane. The middle figure is the expanded diagram at the latitude and longitude where the CJPL is located. The upper and lower plots are for 2° (220 km) north and south of the CJPL, respectively.

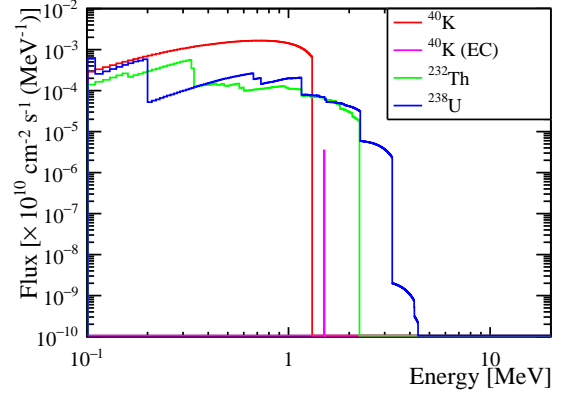


FIG. 4: Electron (anti)neutrino flux prediction at Jinping.

it is a neutrino or antineutrino). Additionally, the scattering angle, which is the deviation from the recoil electron's direction to the incident neutrino's direction, is a function of the neutrino energy E_ν and the recoil electron kinetic energy T_e :

$$\theta = \arccos\left(\frac{1 + m_e/E_\nu}{\sqrt{1 + 2m_e/T_e}}\right), \quad (8)$$

which is used in the subsequent directionality analysis. The total scattering event spectrum is shown in Fig. 5.

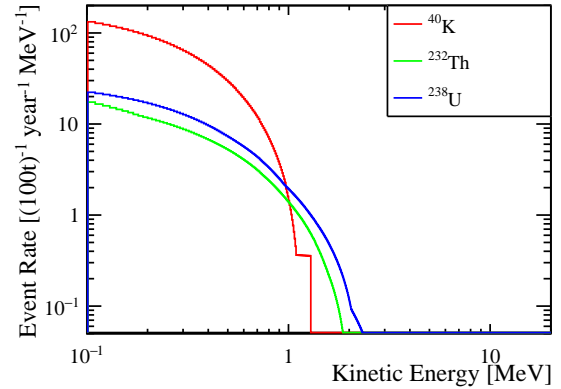
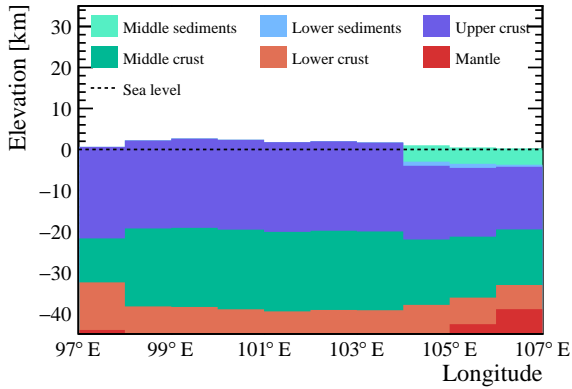


FIG. 5: Total recoil electron spectrum prediction for geoneutrino at Jinping.

G. Solar neutrino background

The intrinsic background of the geoneutrino signal in neutrino-electron elastic scattering is from the solar neutrino. The solar neutrino flux and recoil electron spectrum are computed, which is the same as the

previous result [11], and the recoil electron spectrum is shown in Fig. 6.

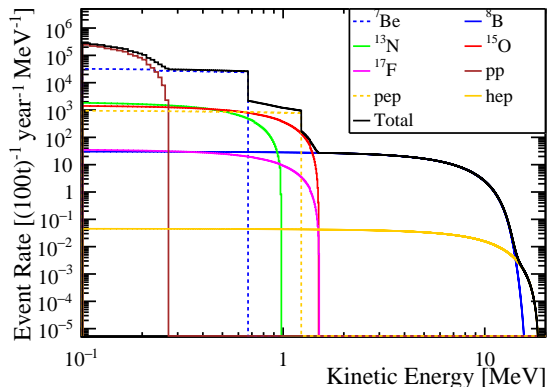


FIG. 6: Total recoil electron spectrum prediction for solar neutrinos at Jinping.

The solar direction is the key to suppressing this background. The Sun's direction varies periodically in the terrestrial coordinate system, showing a daily minor cycle and an annual major cycle. As shown in Fig. 7, the Sun's direction is plotted in the terrestrial coordinate system, where its daily trajectory forms a continuous curve spanning the azimuthal range from $\phi_{\oplus} = -\pi$ to $\phi_{\oplus} = \pi$. The curves corresponding to the winter and summer solstices define the boundaries. The solar neutrinos in this directional band have the chance to be parallel to the geoneutrinos, resulting in a substantial solar neutrino background.

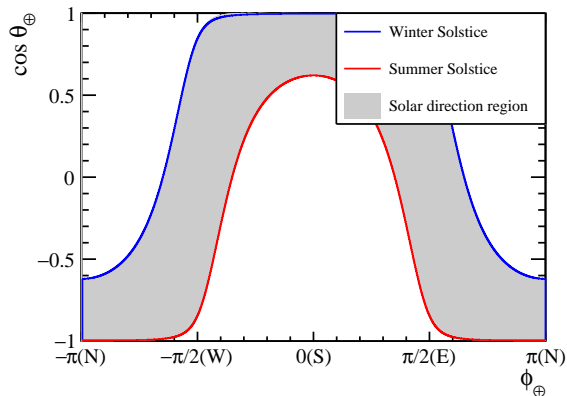


FIG. 7: The evolution distribution of the terrestrial coordinate $\cos \theta_{\oplus}$ and ϕ_{\oplus} of the solar neutrinos. The blue solid line represents the trajectory at the winter solstice, while the red solid line shows that at the summer solstice. The gray area represents the band regions at the other time.

III. DETECTOR RESPONSE SIMULATION

A. Detector setup and simulation

We adopted the detector scheme as in Ref. [11], which is a popular arrangement with liquid scintillators, as in the KamLAND, Borexino, and SNO+ experiments. The center of the detector is the main liquid scintillator, which is contained in a transparent sphere, i.e., an acrylic shell. Surrounding the sphere are the photomultiplier tubes (PMTs), which collect the optical photons emitted during the Cherenkov and scintillation process of charged particles. In the Geant4 simulation [20, 21], the electromagnetic and optical processes are turned on, the incident electrons with energy from 0 to 5 MeV are produced in the liquid scintillator sphere, and the hit time of each photoelectron is recorded for subsequent reconstruction. In the previous study [11], the number of protons of carbon was set to 12 in the Geant4 simulation, and this caused a much worse electron direction smearing than reality.

B. Cherenkov liquid scintillator

There are several Cherenkov liquid scintillator candidates, which all have a long scintillation emission time and a reasonable light yield [3, 12, 22]. In this research, we chose the one with a rise time of 12 ns. The light curve of the liquid scintillator is shown in Fig. 8.

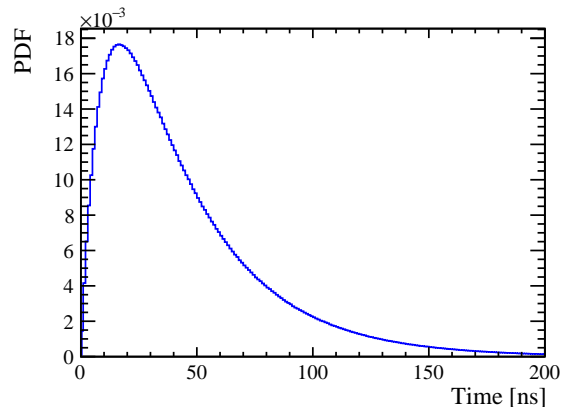


FIG. 8: Scintillation light emission curve of the Cherenkov liquid scintillator.

The critical technical performance for directionality measurement is hindered by the recoil electron scattering process in the liquid scintillator. The choice of a particular Cherenkov liquid scintillator is not a fundamental factor, because they all have similar density and element composition [3, 12], and the capability for direction reconstruction [13] is stable in a certain range.

C. Detector response

In this work, we use a PMT's photo cathode coverage rate of 66% and a quantum efficiency of about 30% in the range of visible photons. So we can collect 20% of the produced photons to reconstruct the energy and direction of the incident particle. We choose the photons produced in the first 2 ns, which are expected to be Cherenkov photons mostly, to reconstruct the direction of the primary electron, \vec{r}_{rec} , as shown in Eq. 9

$$\vec{r}_{\text{rec}} = \frac{1}{N_p} \sum_{i=1}^{N_p} \vec{r}_i, \quad (9)$$

in which the \vec{r}_i stands for the direction of the i -th photon.

For typical 1 MeV electrons, the cosine of the angle between the reconstruction direction and the true direction is shown in Fig. 9.

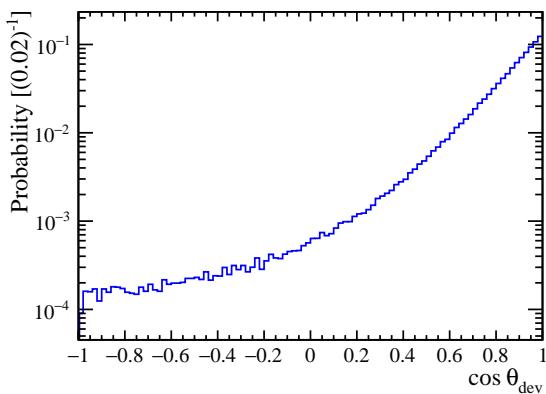


FIG. 9: The cosine of the angle between the reconstruction direction and the true direction for 1 MeV electrons.

With the simulation and the reconstruction, the angular response of the detector as a function of the kinetic energy of the incident electrons is shown in Fig. 10.

IV. SELECTION CRITERIA

A. Geo-solar ratio and energy region selection

Three energy regions are selected for the research of geoneutrinos from different elements based on optimizing the geo-solar signal ratio, which is shown in Fig. 11. The first region of interest, RoI_{K} , covers an energy range of 0.7 MeV to 1.1 MeV, in which the geoneutrinos from ^{40}K are dominant. Similarly, $\text{RoI}_{\text{U/Th}}$ covers an energy region of 1.1 MeV to 2.3 MeV, and is dominated by ^{238}U and ^{232}Th geoneutrinos. RoI_{Geo} covers an energy region of 0.7 MeV to 2.3 MeV, which contains almost all the

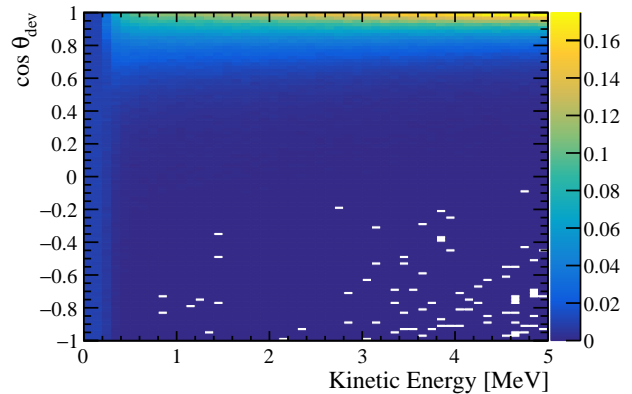


FIG. 10: Angular response as a function of the kinetic energy of the incident electrons. As the kinetic energy of the incident electron decreases, its angular information degrades, and when the energy falls below 0.2 MeV, the Cherenkov threshold, the directional reconstruction capability completely disappears.

geoneutrino signals. In RoI_{K} and $\text{RoI}_{\text{U/Th}}$, the dominant background components are ^7Be , pep and ^{15}O neutrinos, while are pep, ^{15}O and ^8B neutrino in $\text{RoI}_{\text{U/Th}}$.

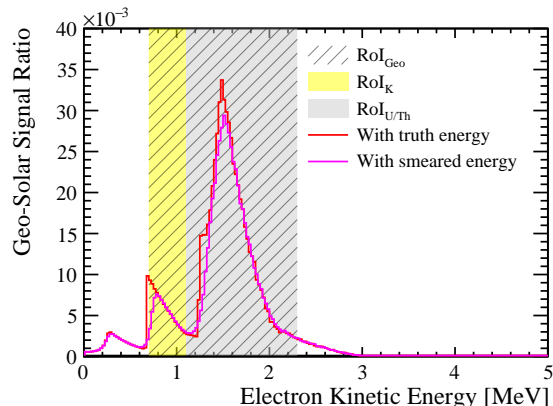


FIG. 11: The ratio of the geoneutrino event rate to that of solar neutrino versus the recoil electron kinetic energy. The red solid line represents the ratio calculated with the true recoil electron kinetic energy, while the magenta solid line represents the ratio calculated with smeared kinetic energy.

B. Neutrino signal direction and solar angle cut

Most of the detected geoneutrinos are emitted from the near-field sediments and upper crust, and some are from the mantle. Due to the rotation and revolution of the Earth, the direction of geoneutrinos has almost

no correlation with the Sun's direction. The angular distributions of the geoneutrinos and the reconstructed electrons are both uniform in solar angle, as presented in Fig. 12 (dashed and solid blue lines). On the other hand, if studied in the terrestrial coordinate system, geoneutrinos gather at $\cos\theta_{\oplus} > 0$. They also show a cluster structure at $0 < \phi_{\oplus} < \pi/2$, manifesting the relatively thicker crust in the Qinghai-Tibet Plateau, which is located northwest of the detector. Fig. 13a and 13c show the $\cos\theta_{\oplus}$ and ϕ_{\oplus} distributions for the geoneutrinos and reconstructed electrons, respectively.

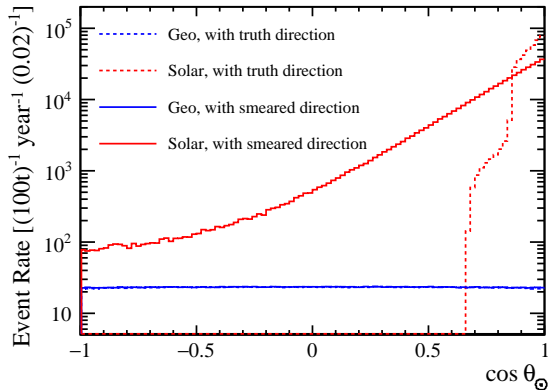


FIG. 12: The solar angle distribution for the geoneutrino signals and solar-neutrino backgrounds. Blue dashed and solid lines represent the distribution of geoneutrino signals with the recoiling electron's kinetic energy in RoI_{Geo} , with true direction and smeared direction, respectively. Similarly, red lines represent the same distributions for solar-neutrino signals. The situation is similar for RoI_{K} and $\text{RoI}_{\text{U/Th}}$.

Solar neutrinos arrive at the Earth in parallel according to the Sun's position at each moment. After the neutrino-electron elastic scattering, the recoil electron will deviate from the true neutrino direction, but, after an energy cut, especially the low energy cut, the tracks with better alignment are selected again for the kinetic reason (see Eq. 8 and the red dashed line of Fig. 12 for RoI_{Geo}). These electrons are scattered in the Cherenkov liquid scintillator, detected with PMTs, and finally reconstructed. The scattering, detection, and reconstruction processes further smear the electron direction and deviate them from the Sun's direction (see the red solid line of Fig. 12 for RoI_{Geo}). If observed in the terrestrial coordinate system, the $\cos\theta_{\oplus}$ and ϕ_{\oplus} of these solar neutrinos have the distribution as in Fig. 13b. The distribution of $\cos\theta_{\oplus}$ and ϕ_{\oplus} of reconstructed electrons is shown in Fig. 13d.

To fully utilize the directionality of the geoneutrino signal and conduct subsequent analysis, the full 4π space in the terrestrial coordinate system is divided into 10×10 solid angle bins. The solar angle cut is optimized in each solid angle bin. For a certain bin i , a critical

cut boundary $\cos\theta_{\text{max}}$ is chosen, and a solar angle cut $\cos\theta_{\odot} < \cos\theta_{\text{max}}$ is applied to all candidates, so as to maximize the local statistical sensitivity, S_i^{loc} ,

$$S_i^{\text{loc}} = N_i^{\text{geo}} / \sqrt{N_i^{\text{geo}} + N_i^{\text{solar}}}, \quad (10)$$

where N_i^{geo} and N_i^{solar} are the numbers of events of the geoneutrino signal and solar neutrino background in the bin i after the $\cos\theta_{\odot}$ cut, respectively. For different solid angle bins having different relative directions to the Earth center and the Sun, the cuts are different. The situations for two example bins are shown in Fig. 14. The first plot represents the optimization result for a typical solid angle bin covered by the sun's trajectory, with $\cos\theta_{\oplus} \in (0.4, 0.6)$ and $\phi_{\oplus} \in (0.4\pi, 0.6\pi)$, which is located in the gray band in Fig. 7. The second plot shows another typical solid angle bin outside the band with $\cos\theta_{\oplus} \in (-0.6, -0.4)$ and $\phi_{\oplus} \in (-0.2\pi, 0)$. The angular distribution of all candidates, including geoneutrinos and solar neutrinos, after the energy and $\cos\theta_{\odot}$ cuts is shown in Fig. 15, in which the reconstructed energy is in RoI_{Geo} , and the exposure is 3 kiloton-years. The event rates before and after the $\cos\theta_{\odot}$ cut in the three energy regions of interest are listed in Tab. I.

V. SENSITIVITY CALCULATION

A. Geoneutrino detection sensitivity

Two methods are applied to calculate the detection sensitivity. A simple one is based on total statistics, and the other uses more detailed information.

Firstly, a total event rate method is used to estimate the detection sensitivity. The total numbers of events of the geoneutrino signal and solar neutrino background after the energy and $\cos\theta_{\odot}$ cuts are obtained as

$$N^{\text{geo}} = \sum_{i=1}^{100} N_i^{\text{geo}}, \quad (11)$$

$$N^{\text{solar}} = \sum_{i=1}^{100} N_i^{\text{solar}},$$

and the uncertainty of the solar neutrino background is determined by

$$\sigma^{\text{solar}} = \sqrt{N^{\text{solar}} + (N^{\text{solar}} \times \sigma^{\text{sys}})^2}, \quad (12)$$

where σ^{sys} represents the relative systematic uncertainty of the solar neutrino background, which includes the uncertainty introduced by the solar neutrino flux and the cut efficiency, and is set to 1.4% as in the previous work. Then, the sensitivity for geoneutrino detection is determined by

$$\text{Sensitivity} = \frac{N^{\text{geo}}}{\sigma^{\text{solar}}}, \quad (13)$$

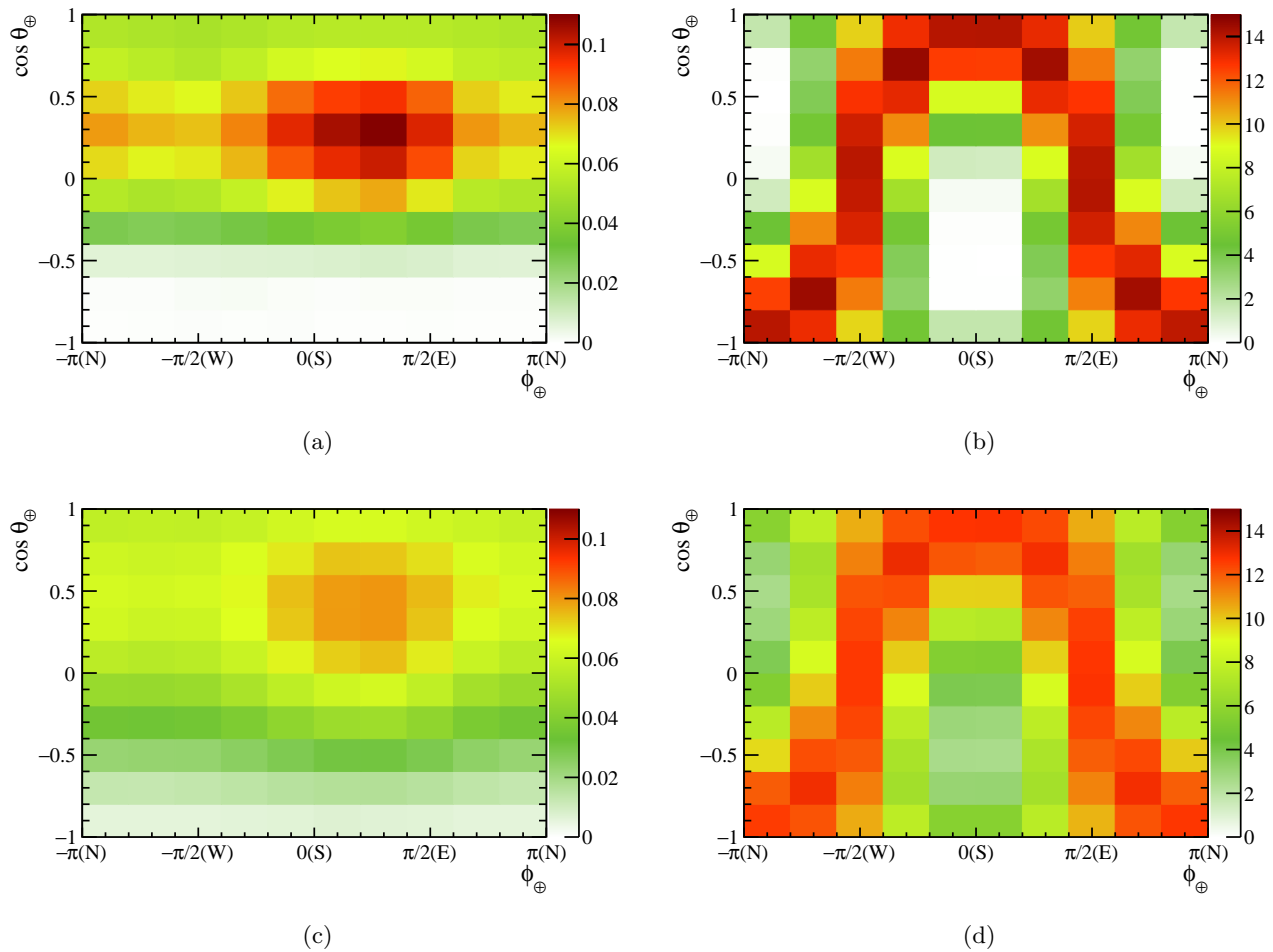


FIG. 13: Angular distributions of the recoil electrons produced by the geoneutrinos and solar neutrinos in RoI_{Geo} . Fig. 13a and Fig. 13b show the true angular distributions for geoneutrinos and solar neutrinos, while Fig. 13c and Fig. 13d show the corresponding reconstructed angular distributions. The z -axis of each panel is shown in units of per 100 ton-years.

	RoI_{Geo}		RoI_{K}		$\text{RoI}_{\text{U/Th}}$	
	Before $\cos\theta_{\odot}$ cut	After $\cos\theta_{\odot}$ cut	Before $\cos\theta_{\odot}$ cut	After $\cos\theta_{\odot}$ cut	Before $\cos\theta_{\odot}$ cut	After $\cos\theta_{\odot}$ cut
^{40}K	57.3	25.2	55.2	24.0	2.3	0.9
^{232}Th	32.7	14.1	23.1	9.9	9.6	4.5
^{238}U	49.8	22.2	32.1	14.1	17.7	8.4
Geoneutrino	139.8	61.5	110.4	48.0	29.4	13.8
Solar neutrino	26532.3	380.4	23383.2	312.6	5240.1	73.5

TABLE I: Number of events for each geoneutrino component at an exposure of 3 kiloton-years, with values shown for both before and after the $\cos\theta_{\odot}$ cut.

which estimates how likely the random fluctuation of the solar neutrino background can reach the number of the geoneutrino signals.

The second method takes the angular difference of the signals and backgrounds into account. A simple-vs-simple likelihood ratio test is applied. A statistic χ^2 is defined based on the Poisson form

likelihood ratio with systematic uncertainty,

$$\chi^2(\vec{n}) = \min \left[-2 \sum_{i=1}^{100} \left(n_i - \lambda_i + n_i \log \frac{\lambda_i}{n_i} \right) + \left(\frac{\eta}{\sigma^{\text{sys}}} \right)^2 \right], \quad (14)$$

where n_i represents the number of candidates in the

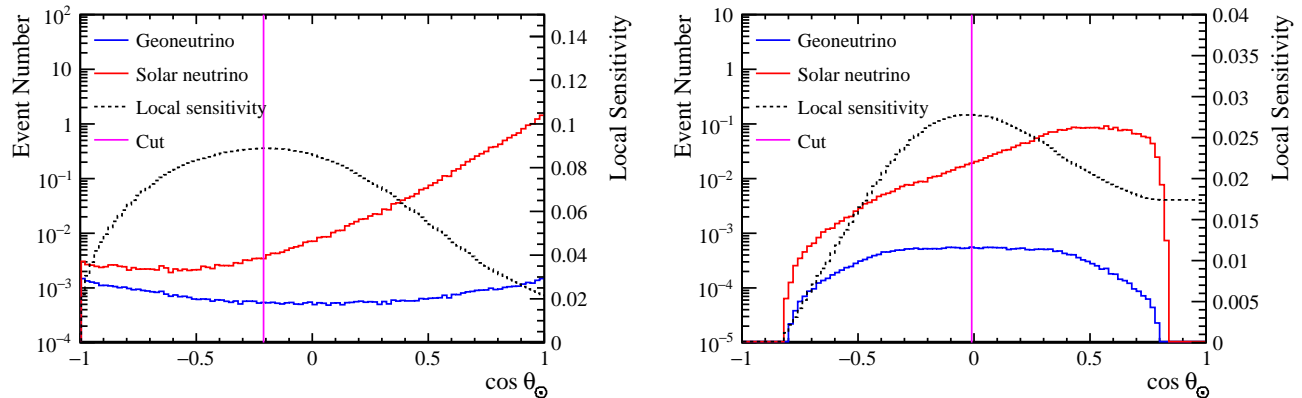


FIG. 14: The $\cos\theta_\odot$ cut is optimized for each solid angle bin. The blue line shows the $\cos\theta_\odot$ distribution for the geoneutrino signals, and the red line shows that of the solar neutrino background. The black dashed line shows the local sensitivity (Eq. 10) variation with the $\cos\theta_\odot$ cut, and the magenta line marks the maximum of the local sensitivity and the selected cut. The first figure represents the result for the solid angle bin at $\cos\theta_\oplus \in (0.4, 0.6)$ and $\phi_\oplus \in (0.4\pi, 0.6\pi)$, while the second one is for the bin of $\cos\theta_\oplus \in (-0.6, -0.4)$ and $\phi_\oplus \in (-0.2\pi, 0)$.

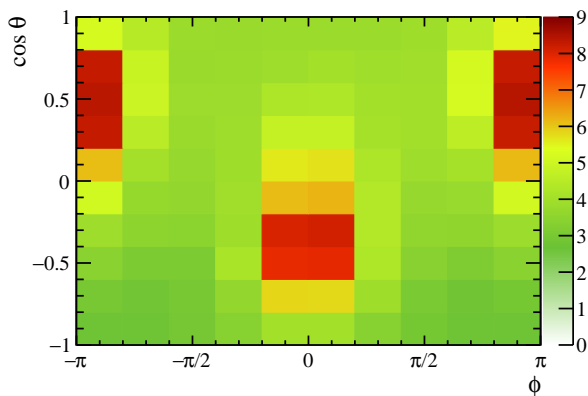


FIG. 15: The terrestrial angle distribution of all expected candidates, including geoneutrinos and solar neutrinos, after the $\cos\theta_\odot$ cut in RoI_{Geo} at an exposure of 3 kiloton-years.

solid angle bin i in a pseudo-experiment, λ_i represents its prediction, and $(\frac{\eta}{\sigma^{\text{sys}}})^2$ is the regularization term introduced by the systematic uncertainty. The prediction depends on the hypothesis, for the hypothesis H_0 with no geoneutrino,

$$\lambda_i = N_i^{\text{solar}} \times (1 + \eta), \quad (15)$$

while for the hypothesis H_1 with the predicted geoneutrino flux obtained in Sec. II,

$$\lambda_i = N_i^{\text{geo}} + N_i^{\text{solar}} \times (1 + \eta). \quad (16)$$

The parameter η is a pull parameter describing the deviation between the fitted number of the solar neutrino background and the prediction, and its uncertainty is

σ^{sys} , which is 1.4 % as in Eq. 12. The simple-vs-simple test statistic can be defined as

$$\Delta\chi^2(\vec{n}) = \chi^2(\vec{n}; H_0) - \chi^2(\vec{n}; H_1). \quad (17)$$

The sensitivity can then be obtained by calculating the p -value via a frequentist approach. 5 million Monte Carlo datasets of both hypotheses are generated. The central value of the number of events in each bin is determined by sampling the systematic uncertainty, and the observed number of events is sampled based on the Poisson statistics. The distribution of $\Delta\chi^2$ at an exposure of 3 kiloton-years in RoI_{Geo} is shown in Fig. 16. The p -value, defined as the probability that the test statistic $\Delta\chi^2$ under the null hypothesis H_0 exceeds the median value of the $\Delta\chi^2$ distribution predicted by the hypothesis H_1 , is calculated and subsequently converted into a sensitivity using the chi-squared distribution function. For the example of 3 kiloton-years exposure in Fig. 16, under the assumption that the null hypothesis H_0 is true, the p -value corresponding to the median value of the $\Delta\chi^2$ distribution predicted by the hypothesis H_1 is 4.2×10^{-4} , corresponding to a sensitivity of 3.53σ . A scan of sensitivity as a function of exposure is performed and presented in Fig. 17.

The same analysis procedure is implemented for RoI_K and RoI_{U/Th}. The sensitivity curves obtained for these two search regions are illustrated in Fig. 18 and Fig. 19.

For comparison, the previous result [11] is also included. The significant improvement from the previous research to this study stems from the problem solved in the detector response simulation in Sec. III A, the optimization of the $\cos\theta_\odot$ cut in each solid angle bin, and the application of the simple-vs-simple likelihood ratio test method. Specifically, to reach a 3σ discovery sensitivity, the required exposure for the three energy

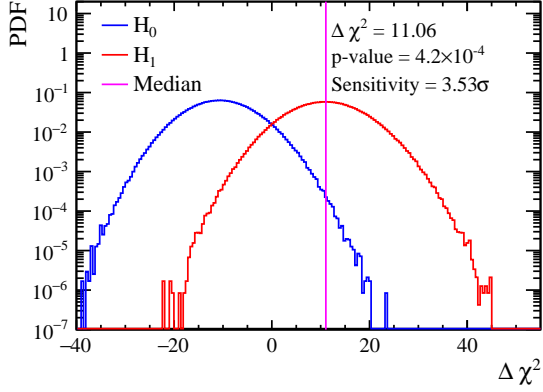


FIG. 16: The test statistic $\Delta\chi^2$ distribution for two sample series under the two hypotheses H_0 (without geoneutrino) and H_1 (with geoneutrinos) at an exposure of 3 kiloton-years.

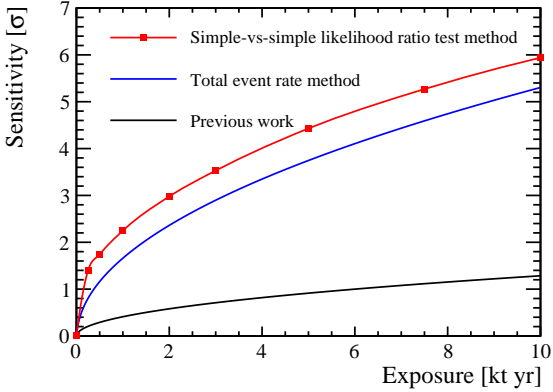


FIG. 17: Sensitivity to detect the geoneutrino signal in RoI_{Geo} . The red solid line represents the sensitivity curve obtained via the nested likelihood ratio test method, the blue solid line represents that obtained via the total event rate method, while the black solid line shows the previous result.

regions of RoI_{Geo} , RoI_{K} , and $\text{RoI}_{\text{U/Th}}$ are 2.0, 2.8, and 6.8 kiloton-years, respectively.

B. The Earth's large-scale structures imaging

With the direction reconstruction, the non-uniformity of the angular distribution of the geoneutrino signal can be observed, thereby making it possible to image the large-scale structures of the Earth's interior. The process is demonstrated below.

An Asimov dataset is generated. The geoneutrino signal is obtained by subtracting the solar neutrino

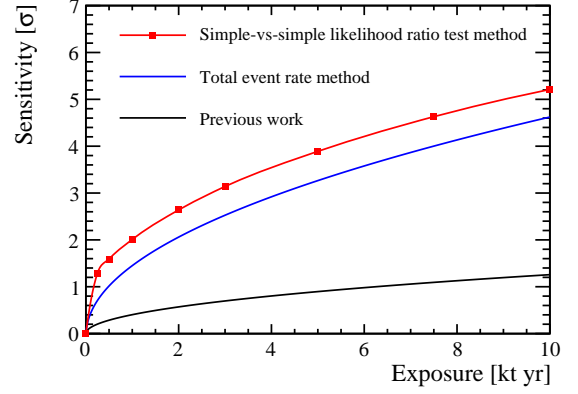


FIG. 18: Sensitivity to detect the geoneutrino signal in RoI_{K} . The legends are the same as Fig. 17.

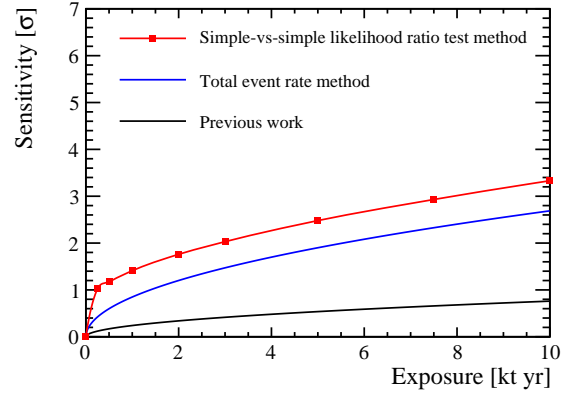


FIG. 19: Sensitivity to detect the geoneutrino signal in $\text{RoI}_{\text{U/Th}}$. The legends are the same as Fig. 17.

background from the candidates, as

$$N_i^{\text{geo}} = N_i^{\text{can}} - N_i^{\text{solar}}, \quad (18)$$

and its uncertainty is

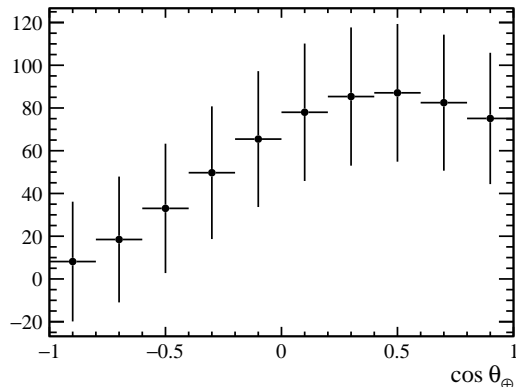
$$\sigma_i^{\text{geo}} = \sqrt{(\sigma_i^{\text{can}})^2 + (N_i^{\text{solar}} \times \sigma_{\text{sys}})^2}. \quad (19)$$

The raw geoneutrino signal's angular distribution, $N_i^{\text{geo,raw}}$ is then got by correcting the cut selection efficiency, ϵ_i^{geo} , in each solid angular bin i as

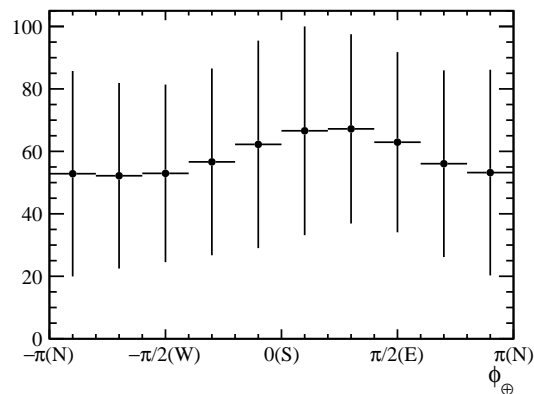
$$N_i^{\text{geo,raw}} = \frac{N_i^{\text{geo}}}{\epsilon_i^{\text{geo}}}. \quad (20)$$

The projections of the raw geoneutrino signal's angular distribution onto the $\cos\theta_{\oplus}$ and ϕ_{\oplus} directions are produced to first reveal the non-uniform structure of the Earth, as shown in Fig. 20. An exposure of 12.5 kiloton-years is adopted in this demonstration. The concentration of the geoneutrino signal at $\cos\theta_{\oplus} > 0$ in

Fig. 20a reflects the geoneutrinos' origin from the Earth, while the bump in the azimuthal ϕ_{\oplus} direction in Fig. 20b is from the Qinghai-Tibet Plateau.



(a)



(b)

FIG. 20: Projections of the geoneutrino signal angular distribution onto the $\cos \theta_{\oplus}$ and ϕ_{\oplus} directions at an exposure of 12.5 kiloton-years, with both the central values and error bars.

The directional non-uniformity detection sensitivity is calculated via the same simple-vs-simple likelihood ratio test method as in Sec. V A. A uniform geoneutrino angular distribution with the same total flux is generated as the hypothesis H_0 . The angular distribution obtained in Sec. II serves as the hypothesis H_1 . The likelihood and test statistic are defined the same as Eq. 14 and Eq. 17. The distributions for both hypotheses are obtained through 5 million pseudo-experiments. For example, at

the exposure of 12.5 kiloton-years, the p -value is 0.0012, and a sensitivity of 3.23σ is obtained. The variation of directional non-uniformity detection sensitivity with exposure is shown in Fig. 21. Specifically, to reach a 3σ sensitivity, the required exposure is 10.6 kiloton-years.

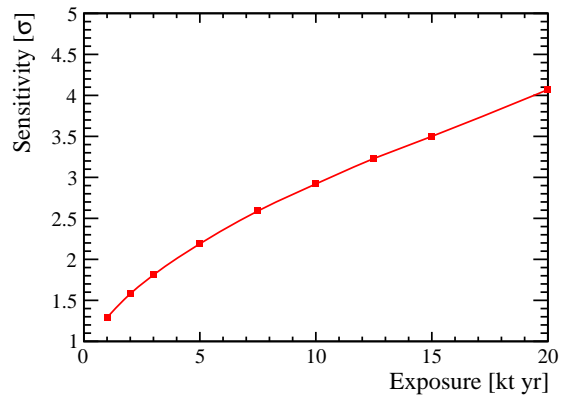


FIG. 21: Sensitivity to detect the geoneutrinos' directional non-uniformity.

VI. SUMMARY

The potential for detecting ^{40}K geoneutrinos and imaging the Earth's large-scale structures is analyzed in this work. Using a combined Earth model that incorporates the CRUST1.0 crust model and a medium-Q mantle model, the event rate of geoneutrino-electron elastic scattering is calculated. A Cherenkov liquid scintillator detector is implemented to simulate the recoil electrons. A problem in the previous study is fixed, and the detector angular response is derived. Geoneutrinos are mainly from the sediments and upper crust, while the intrinsic background, solar neutrinos, is aligned with the Sun's position. The full 4π space in the terrestrial coordinate system is divided into 100 solid angle bins, and an optimized solar angle cut is achieved independently for each bin by maximizing the local signal-to-background ratio. Analyses are performed for the three energy regions, i.e., for all, potassium, and uranium and thorium geoneutrinos, respectively. The geoneutrino detection sensitivity is improved. The 3σ sensitivity to discover the potassium-40 geoneutrinos is 2.8 kiloton-years. With the direction information, an image of the Earth's large-scale structures can also be made, and the required exposure is 10.6 kiloton-years to reject a uniform geoneutrino distribution by 3σ .

[1] G. Bellini *et al.*, Geo-neutrinos, *Prog. Part. Nucl. Phys.* **73**, 1 (2013).

[2] W. F. McDonough, O. Šrámek, and S. A. Wipperfurth, Radiogenic power and geoneutrino luminosity of the Earth and other terrestrial bodies through time,

- Geochem. Geophys. Geosyst. **21**, e2019 (2020).
- [3] Z. Guo *et al.*, Slow liquid scintillator candidates for MeV-scale neutrino experiments, *Astropart. Phys.* **109**, 33 (2019).
- [4] O. Šrámek *et al.*, Revealing the Earth’s mantle from the tallest mountains using the Jinping Neutrino Experiment, *Sci. Rep.* **6**, 33034 (2016).
- [5] L. Wan, G. Hussain, Z. Wang, and S. Chen, Geoneutrinos at Jinping: Flux prediction and oscillation analysis, *Phys. Rev. D* **95**, 053001 (2017).
- [6] T. Araki *et al.*, Experimental investigation of geologically produced antineutrinos with KamLAND, *Nature* **436**, 499 (2005).
- [7] A. Gando *et al.* (KamLAND), Partial radiogenic heat model for Earth revealed by geoneutrino measurements, *Nature Geo.* **4**, 647 (2011).
- [8] M. Agostini *et al.* (Borexino Collaboration), Comprehensive geoneutrino analysis with Borexino, *Phys. Rev. D* **101**, 012009 (2020).
- [9] M. Abreu *et al.* (SNO + Collaboration), Measurement of reactor antineutrino oscillation at SNO+, *Phys. Rev. Lett.* **135**, 121801 (2025).
- [10] P. Vogel and J. F. Beacom, Angular distribution of neutron inverse beta decay, $\bar{\nu}_e + p \rightarrow e^+ + n$, *Phys. Rev. D* **60**, 053003 (1999).
- [11] Z. Wang and S. Chen, Hunting potassium geoneutrinos with liquid scintillator Cherenkov neutrino detectors, *Chin. Phys. C* **44**, 033001 (2020).
- [12] S. D. Biller, E. J. Leming, and J. L. Paton, Slow fluors for effective separation of Cherenkov light in liquid scintillators, *Nucl. Instrum. Meth. A* **972**, 164106 (2020).
- [13] W. Luo *et al.*, Reconstruction algorithm for a novel Cherenkov scintillation detector, *JINST* **18** (02), P02004.
- [14] E. Sanshiro, *Neutrino Geophysics and Observation of Geo-neutrinos at KamLAND*, Phd thesis, Tohoku University (2005).
- [15] G. Laske, G. Masters, Z. Ma, and M. Pasyanos, Update on CRUST1.0 - a 1-degree global model of Earth’s crust, in *EGU General Assembly Conference Abstracts*, EGU General Assembly Conference Abstracts (2013) pp. EGU2013–2658.
- [16] Y. Huang *et al.*, A reference Earth model for the heat-producing elements and associated geoneutrino flux, *Geochem. Geophys. Geosyst.* **14**, 2003 (2013).
- [17] A. M. Dziewonski and D. L. Anderson, Preliminary reference Earth model, *Phys. Earth Planet. Interiors* **25**, 297 (1981).
- [18] S. Navas *et al.* (Particle Data Group Collaboration), Review of particle physics, *Phys. Rev. D* **110**, 030001 (2024).
- [19] C. Giunti *et al.*, *Fundamentals of Neutrino Physics and Astrophysics* (Oxford University Press, 2007).
- [20] J. Allison *et al.*, Recent developments in Geant4, *Nucl. Instrum. Meth. A* **835**, 186 (2016).
- [21] J. Allison *et al.*, Geant4 developments and applications, *IEEE Trans. Nucl. Sci.* **53**, 270 (2006).
- [22] M. Li *et al.*, Separation of scintillation and Cherenkov lights in linear alkyl benzene, *Nucl. Instrum. Meth. A* **830**, 303 (2016).